Plasma Physics and Controlled Fusion

PAPER

Identification of trapping finer-scale fluctuations in a solitary vortex in linear magnetized plasma

To cite this article: Hiroyuki Arakawa *et al* 2023 *Plasma Phys. Control. Fusion* **65** 115002

Plasma Phys. Control. Fusion 65 (2023) 115002 (10pp) https://doi.org/10.1088/1361-6587/acfbb3

Identification of trapping finer-scale fluctuations in a solitary vortex in linear magnetized plasma

Hiroyuki Arakawa[1,*], **Makoto Sasaki**[2], **Shigeru Inagaki**[3,4], **Maxime Lesur**[5], **Yusuke Kosuga**[4,6], **Tatsuya Kobayashi**[6,7], **Fumiyoshi Kin**[3], **Takuma Yamada**[4,8], **Yoshihiko Nagashima**[6], **Akihide Fujisawa**[4,6] and **Kimitaka Itoh**[4,7,9]

[1] Department of Health Sciences, Faculty of Medical Sciences, Kyushu University, Fukuoka 812-8582, Japan
[2] College of Industrial Technology, Nihon University, Narashino 275-8575, Japan
[3] Institute of Advanced Energy, Kyoto University, Uji 611-0011, Japan
[4] Research Center for Plasma Turbulence, Kyushu University, Kasuga 816-8580, Japan
[5] Université de Lorraine, CNRS, IJL, Nancy F-54000, France
[6] Research Institute for Applied Mechanics, Kyushu University, Kasuga 816-8580, Japan
[7] National Institute for Fusion Science, National Institutes of Natural Sciences, Toki 502-5292, Japan
[8] Faculty of Arts and Science, Kyushu University, Fukuoka 819-0395, Japan
[9] Chubu University, Kasugai, 487-8501, Japan

E-mail: arakawa.hiroyuki.306@m.kyushu-u.ac.jp

Received 2 July 2023, revised 19 August 2023
Accepted for publication 20 September 2023
Published 28 September 2023

Abstract

The mutual interaction of drift wave-type modes and zonal flows causes the formation of higher-order nonlinear structures. This study focuses on the spatio-temporal behavior of these higher-order structures in a linear magnetized plasma. The structures include a solitary vortex, a long-lived circumnavigating motion localized both radially and azimuthally, and a short-lived packet of finer-scale fluctuations excited at the position of the solitary vortex. Observing the time evolution of the two-dimensional cross-sectional structures revealed that the packet of finer-scale fluctuations is trapped in the solitary vortex. The trapping times found are consistent with the theoretical evaluation.

Keywords: magnetized plasma, zonal flow, solitary vortex, finer-scale fluctuations, higher-order nonlinear structure, two-dimensional cross-sectional structure

(Some figures may appear in colour only in the online journal)

1. Introduction

Dynamic interactions between linearly unstable drift wave and secondarily nonlinearly generated zonal flows [1, 2] have been actively investigated in plasma turbulence owing to its significant influence on plasma transport [3–5]. Geodesic acoustic modes (GAMs), an oscillating branch of zonal flows specific to toroidal plasmas, have also been the subject of many studies [6]. The physics related to the interaction between drift-wave and zonal flows is considered to share a common, somewhat universal nature, at least from linear magnetized plasmas to toroidal fusion plasmas. Consequently, research has been advanced in fundamental linear magnetized plasmas. For instance, investigations into the intrinsic nature of drift waves [7], transitions from drift wave to turbulence [8], direct observations of zonal flow generation [9], and interactions between drift wave and zonal flows [10–13] have been conducted.

* Author to whom any correspondence should be addressed.

Theoretical and simulation studies suggest that spatio-temporal dynamics of drift waves interacting with zonal flows can be significantly influenced by the trapping of higher-order, nonlinearly excited coherent structures. The trapping in zonal flows has been found by Kaw *et al* [14], as a result of phase-space dynamics (formation of coherent vortex in the phase-space). The trapping mechanism has also been applied to the interaction between drift wave and GAMs [15–17]. In this context, the spatial localization of the structures by the stationary zonal flows [18], and the azimuthal bunching of the structures by the streamer [19] have been found to be caused by the trapping. The trapping mechanism is independent of magnetic field configurations, so that it should be possible to validate the mechanism in linear magnetized plasmas. However, the trapping of the structures has not yet been directly observed experimentally and as such should be demonstrated.

Our recent experimental studies of linear magnetized plasma observed higher-order coherent structures in the system of drift wave-type modes and the secondary nonlinearly generated zonal flow [20]. The higher-order structures includes a spatially localized, long-lived solitary vortex and short-lived packet of finer-scale fluctuations. The solitary vortex is excited by the interaction between the drift wave-type modes and the zonal flow [21]. The finer-scale fluctuations (termed 'splash' in [20]) have shorter lifetimes and excited at the same azimuthal position as the solitary vortex [20]. However, the finer-scale fluctuations were only observed at a specific radial position, and temporal variations in the two-dimensional cross-sections had not been obtained.

In this study, we experimentally identified the trapping of the finer-scale fluctuations in a solitary vortex in linear magnetized plasma. The time-resolved two-dimensional analysis allows us to observe linearly unstable drift wave-type modes and the secondary nonlinearly generated zonal flow, as well as the solitary vortex and the short-lived packet of finer-scale fluctuations. The trajectory of the finer-scale fluctuations circulating in the solitary vortex is detected, demonstrating that they are trapped in the solitary vortex. The time at which finer-scale fluctuations were trapped was in close agreement with the theoretical evaluation.

2. Experimental setup

A cylindrical argon plasma with a diameter of $\sim$0.1 m and an axial length of 3.74 m was produced at a linear plasma device, LMD-U [20]. The plasma was excited by radio frequency (RF) waves and was radially bounded by a magnetic field with no external source of momentum. The operational parameters are 3 kW RF power, 900 G magnetic field strength (B), and 0.68 Pa argon gas pressure. Typical plasma parameters are central plasma density of $\sim 6 \times 10^{18}\,\mathrm{m}^{-3}$ and $\sim$2.5 eV electron temperature (T_e). The major diagnostic tools used in this study are two multi-channel arrays of Langmuir probes. One is an azimuthal array with 64 probes located at a radius of $r = 4$ cm, which is the position where the density gradient is at its maximum. Another array consists of three radially movable probes with a range of $r = 1.5$–7 cm. The Langmuir probes measure the ion saturation current (I_is) and the floating potential (V_f), which are roughly proportional to the electron density and the plasma potential, respectively. These measures are obtained simultaneously during each discharge (0.5 s) and sampled at a frequency of 1 MHz.

3. Fundamental observations

Figure 1(a) shows the dependence in time and azimuthal angle of I_is at $r = 4$ cm by the azimuthal probe array. The steep density peeks steadily propagates in the electron diamagnetic direction. The fundamental mode ($m = 1, f_\mathrm{DW} = 1.2$ kHz) and its higher harmonics have the same phase velocity, where m is the azimuthal mode number, which is related to the wavenumber (k_θ) via the expression, $m = rk_\theta$. As the fundamental mode is observed in a region with a steep density gradient ($\nabla n/n \sim 100\,\mathrm{m}^{-1}$). The linear dispersion relation of the drift wave is given by $f_\mathrm{DW} = (k_\theta \frac{T_\mathrm{e}}{eB}\frac{\nabla n}{n})/(1+\rho^2 k_\theta^2)\cdot\frac{1}{2\pi} \sim 1.8$ kHz, which aligns closely with our experimental observation of f_DW. Consequently, the mode is considered to be of the drift wave-type. Here, the drift wave-type mode and its harmonics is referred to as the waves.

To understand how the solitary vortex and the packet of finer-scale fluctuations are excited, a Galilean transform is applied to figure 1(a); the linear phase shift in the azimuthal angle along the propagation direction of the waves are subtracted. The results are shown in figure 1(b). The red and yellow arrows in the figure display the density peaks of the solitary vortex and packet of finer-scale fluctuations. The solitary vortex and the packet of finer-scale fluctuations propagate at $2.6 \times 10^3\,\pi\,\mathrm{rad\,s}^{-1}$ and $4 \times 10^3\,\pi\,\mathrm{rad\,s}^{-1}$, respectively, in the laboratory frame. A frequency filter ($<$1 kHz or $>$1 kHz) was applied to figure 1(b) at the transformed azimuthal angle $\theta' = 0.9\,\mathrm{rad}\,2\pi^{-1}$ and was demonstrated in figures 1(c) and (d). The excitation/damping of the density in the solitary vortex and the amplitude envelope of the finer-scale fluctuations are synchronized at a frequency of $\sim$0.4 kHz. The temporal evolution of the floating potential fluctuation (0.1–1 kHz) at $r = 4$ cm by the radially movable is shown in figure 1(e). The figure indicates that the potential is also synchronized with the frequency of the solitary vortex and the amplitude envelope of the finer-scale fluctuations. Our previous studies reveal the existence of the zonal flow in these experimental conditions [20, 22]. The zonal flow has a frequency of about 0.4 kHz and a radial wavenumber of $0.8\pi\,\mathrm{rad\,cm}^{-1}$. Compared to the typical period of the waves, the solitary vortex has a long lifetime ($\sim$1.2 ms, which is equal to half of the typical zonal flow period), while the packet of finer-scale fluctuations has a short lifetime (around 0.2 ms at this radius).

As the zonal flow and the waves interact, the waveform of the waves is modified by the frequency of the zonal flow as it propagates [21]. This change stems from the modulation of the fundamental mode, which subsequently affects the amplitude

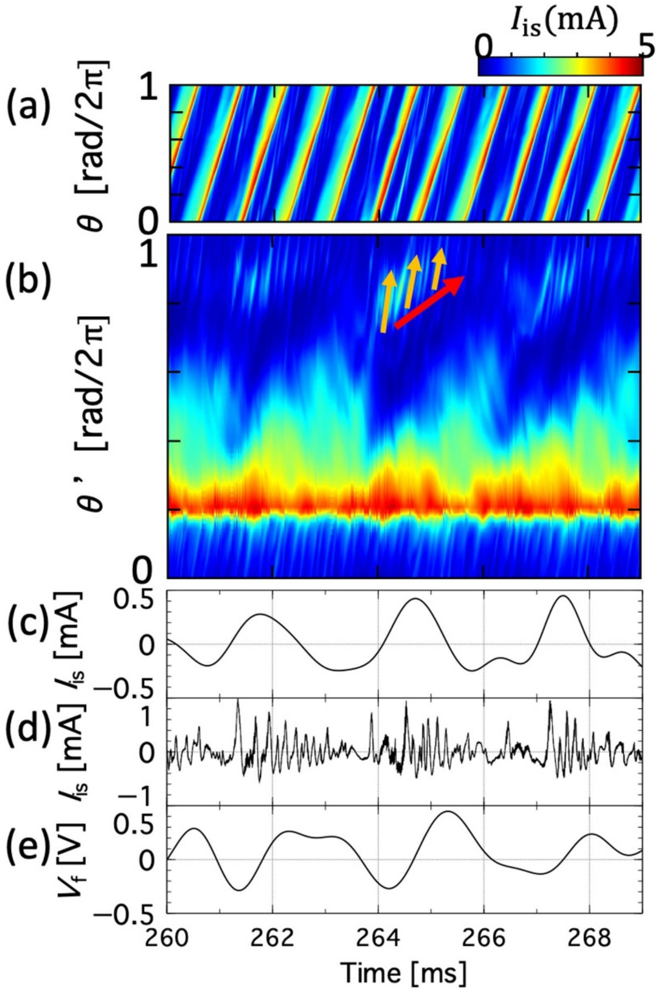

Figure 1. (a) Spatio-temporal behavior of the ion saturation current (I_{is}) at a radius of $r = 4$ cm. The positive direction of the vertical axis corresponds to the electron diamagnetic direction. (b) Galilean transformed (a). The azimuthal angle (θ) of the vertical axis in (a) is transformed to $\theta' = \theta - v_p t$, where v_p denotes the phase velocity of the nonlinear wave. The red arrow indicates the propagation of a solitary vortex and the yellow arrows highlight the propagation of the packet of finer-scale fluctuations. (c) Temporal behavior of I_{is} for the solitary vortex (d) and for the packets of finer-scale fluctuations. (e) Temporal behavior of V_f of the zonal flow.

and phase relationship with the harmonic waves. This leads to the formation of a solitary vortex [21]. The excitation of finer-scale fluctuations is also synchronized with this process.

4. Reconstruction of two-dimensional structure

To understand the propagation in the radial-azimuthal cross-section of the finer-scale fluctuations, a modified template method was used with the data collected from the azimuthal probe array and the radially movable probe array. The template method [23] is a technique of conditional averaging of structures based on the correlation coefficient between a reference waveform and the time-varying waveform. The modified template method is a two-dimensional extension of the one-dimensional template method for structure extraction in turbulence.

Here, the reference waveform was generated in the following iterative manner [23]. Initially, the reference waveform was a cosine function that was uniform in the azimuthal angle, as illustrated in figure 2(a). The cross-correlation function between this initial reference waveform (denoted as $N = 0$, figure 2(a)) and the spatio-temporal I_{is} from the azimuthal probe array (figure 2(f)) was calculated. For this analysis, we selected a specific azimuthal range, $\theta' = 0.78$–1.0 rad $2\pi^{-1}$, to include the solitary vortex and the packet of finer-scale fluctuations, and used data from the last 0.3 s of a 0.5 s single discharge within the spatio-temporal I_{is}. Peak times from the cross-correlation were identified, as marked by the red points in figure 2(g). Using these peak times as a focal point, the subsequent reference waveform was obtained by averaging the relevant spatio-temporal I_{is} (figure 2(b)). This process was repeated: for example, peak times from the cross-correlation between the updated reference waveform ($N = 1$, figure 2(b)) and the spatio-temporal I_{is} (figure 2(f)) were identified in figure 2(h). The next iteration for the waveform was then produced, as shown in figure 2(c) for $N = 2$. This iterative refinement continued until the 50th reference waveform, which had

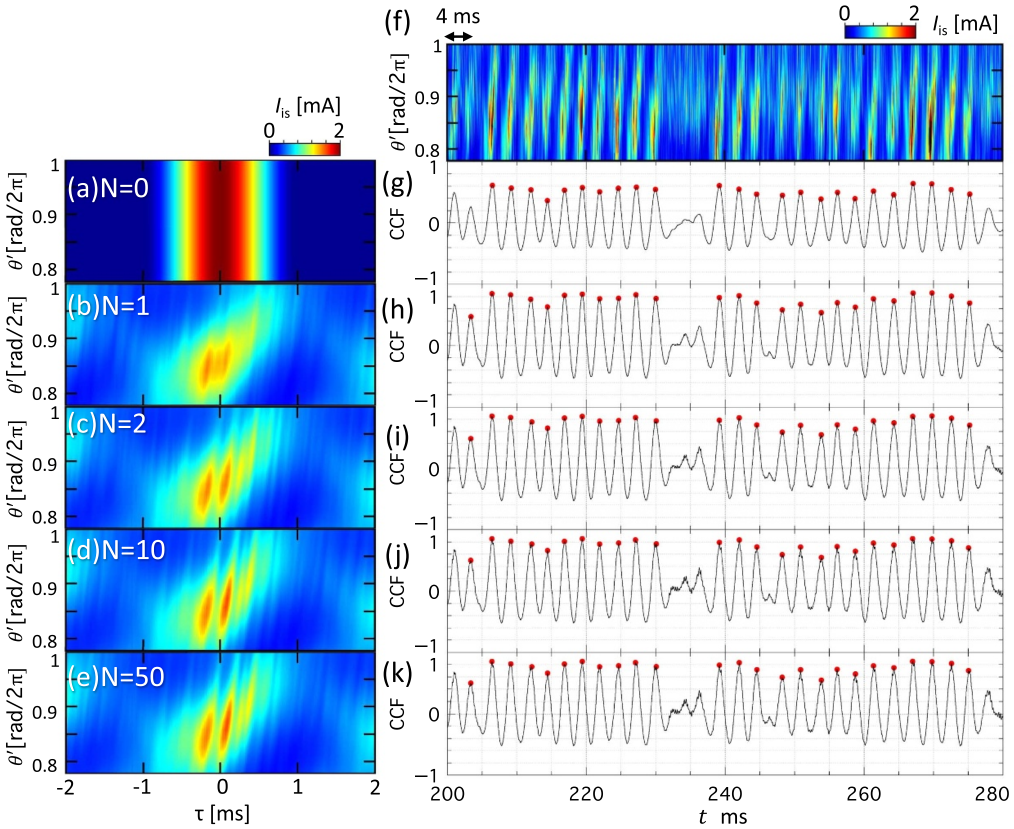

Figure 2. The process of two-dimensional reference waveform generated by the template method. (a)–(e) Iterative reference waveform with $N = 0$, 1, 2, 10 and 50, where N denotes the iteration number. The resulting reference waveform is (e). (f) Spatio-temporal I_{is} of a partial azimuthal range, $\theta' = 0.78–1.0\,\mathrm{rad}\,2\pi^{-1}$, where the Galilean transform was applied. (g)–(k) Cross-correlation function (CCF) between the Nth reference waveform and spatio-temporal I_{is} (f). The red points indicate the correlation peaks.

achieved convergence (as demonstrated in appendix A). The resulting reference waveform is shown in figure 2(e).

The method of reconstructing a cross-sectional structure using the reference waveform is shown below [20]. A visualized explanation is available in appendix B. The time, t_0, was calculated as the point in time when the correlation occurred between the reference waveform and the spatio-temporal I_{is} of the solitary vortex and the packet of finer-scale fluctuations, where the Galilean transform is applied on the azimuthal probe array data. The delay time for the ith period, τ, was defined by the equation $\tau = t - t_0(i)$. The relative azimuthal location of the radially movable probe array with respect to the correlation peak of the azimuthal probe array data, θ_i, was also identified. Values from the radially movable probe array were measured simultaneously at various radial positions. For each radius, we reconstructed the azimuthal-temporal structure via the conditional averaging of the values from the radially movable probe array with respect to θ_i and τ. Here, the I_{is} and V_{f} of the radially movable probe array are normalized as $\tilde{I}_{\mathrm{is}}/\bar{I}_{\mathrm{is}}$ and $eV_{\mathrm{f}}/T_{\mathrm{e}} \equiv \phi$, where the $\tilde{}$ and $\bar{}$ represent fluctuation components or time averages at each radial position. Thereafter, ϕ denotes the normalized potential. Combining the azimuthal-temporal structure of all the radial positions, an entire region of the cross-sectional structure, $\tilde{I}_{\mathrm{is}}/\bar{I}_{\mathrm{is}}(\theta, r, \tau)$ or $\phi(\theta, r, \tau)$, was obtained.

The cross-sectional zonal potential was obtained by filtering the $m = 0$ signal from each radial and temporal component. Singular value decomposition (SVD) analysis was used to determine the other components [24, 25]. The waves and the solitary vortex varied with the frequency of the zonal flow (~0.4 kHz); as a result, the structures were reconstructed by adding the temporally varying structures at 0.4 kHz and its harmonic at 0.8 kHz. The packet of finer-scale fluctuations was then reconstructed by including the structures in the order of the largest singular value of the SVD modes and considering the dimension with the highest correlation coefficient with the azimuthal probe array. The other SVD modes were treated as noise and were therefore not considered in this analysis. The Galilean transformation, which subtracts the linear phase shift of the azimuthal angle along the direction of the wave propagation, is used to make the changes in the reconstructed structures more clearly.

5. Time evolution of two-dimensional spatial structure

Figure 3(a) shows the temporal behavior of the zonal flow ($m = 0$ fluctuation), $V_{\mathrm{ZF}} \equiv \rho \partial\phi/\partial r$, where $\rho = c_{\mathrm{s}}/\omega_{\mathrm{Ci}} = (eT_{\mathrm{e}}/m_{\mathrm{i}})^{1/2}/(eB/m_{\mathrm{i}}) \approx 1.1$ cm is the Larmor radius, c_{s} is the

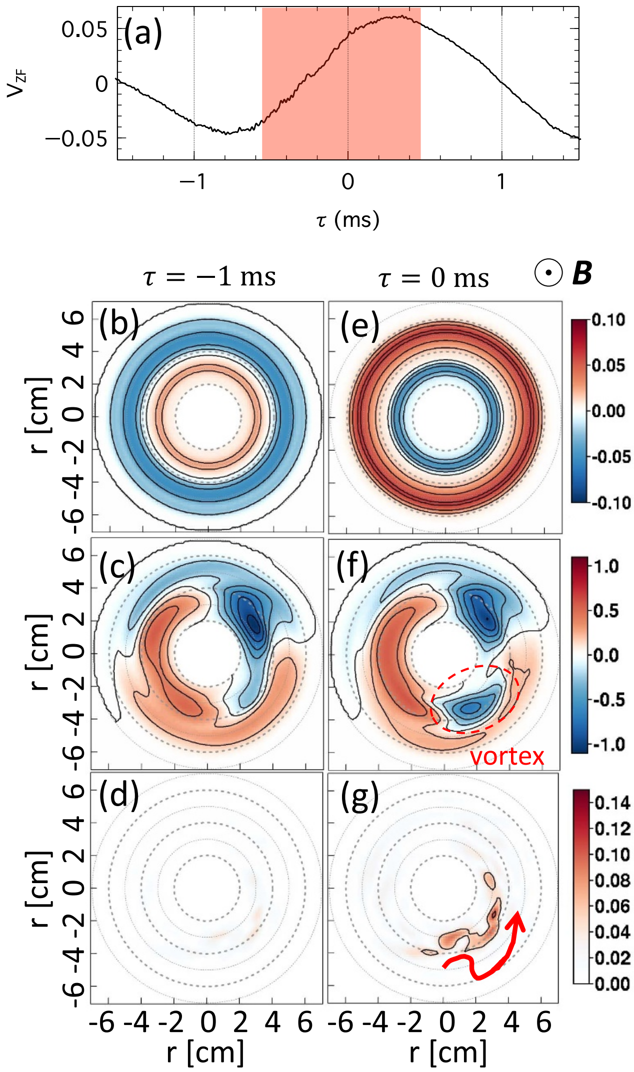

Figure 3. (a) Temporal behavior of the zonal flow ($r = 3$–4.5 cm). The hatched region shows the time in the excitation of the solitary vortex and the packet of finer-scale fluctuations. (b)–(g) Two-dimensional structure of potential fluctuations for the zonal flow (b) and (e), the waves and the solitary vortex (c) and (f), and the amplitude envelope of the packet of finer-scale fluctuations (d) and (g). (b)–(d) show the structures at $\tau = -1$ ms, and (e)–(g) show the structures at $\tau = 0$ ms. The red arrow in (g) indicates the propagation direction of the packet of finer-scale fluctuations.

ion sound velocity, $\omega_{\mathrm{C_i}}$ is the ion gyro frequency and m_{i} is the mass of argon ($\approx 6.63 \times 10^{-26}$ kg). The two-dimensional azimuthal cross-section image of the potential fluctuation $\tilde{\phi}$ at $\tau = -1$ ms and $\tau = 0$ ms, averaged over a time interval of 0.4 ms, are shown in figures 3(b)–(g). Figures 3(b) and (e) show the zonal flow potential, figures 3(c) and 1(f) show the waves and the solitary vortex, respectively, and figures 3(d) and (g) demonstrate the amplitude envelope of the finer-scale fluctuations. The closed isolines of $\tilde{\phi}$, highlighted in figure 3(f) by the dashed ellipse, show the excitation of the solitary vortex because in figure 3(c) the $\tilde{\phi}$ at this location is neither closed nor excited. The large amplitude in figure 3(g) indicates a packet of finer-scale fluctuations being excited, while a small amplitude in figure 3(d) shows that it is not excited. The excitation location of the packet of finer-scale fluctuations is equal to that of the solitary vortex, with a $\sim$5 cm in the azimuthal direction and a $\sim$3 cm in the radial direction. The red arrow next to the fluctuations in figure 3(g) indicates the direction of propagation for the finer-scale fluctuation, as shown below.

6. Trapping of the packet of finer-scale fluctuations

The packet of finer-scale fluctuations is trapped by the solitary vortex. Figure 4 shows the time variation in the two-dimensional potential structure of the packet of finer-scale fluctuations. Figures 4(a)–(f) are time-averaged snapshots for 10 μs each and show the time at (a) $\tau = -330\,\mu$s, (b) $\tau = -250\,\mu$s, (c) $\tau = -220\,\mu$s, (d) $\tau = -170\,\mu$s, (e) $\tau = -130\,\mu$s, and (f) $\tau = -50\,\mu$s respectively. The filled contour indicates

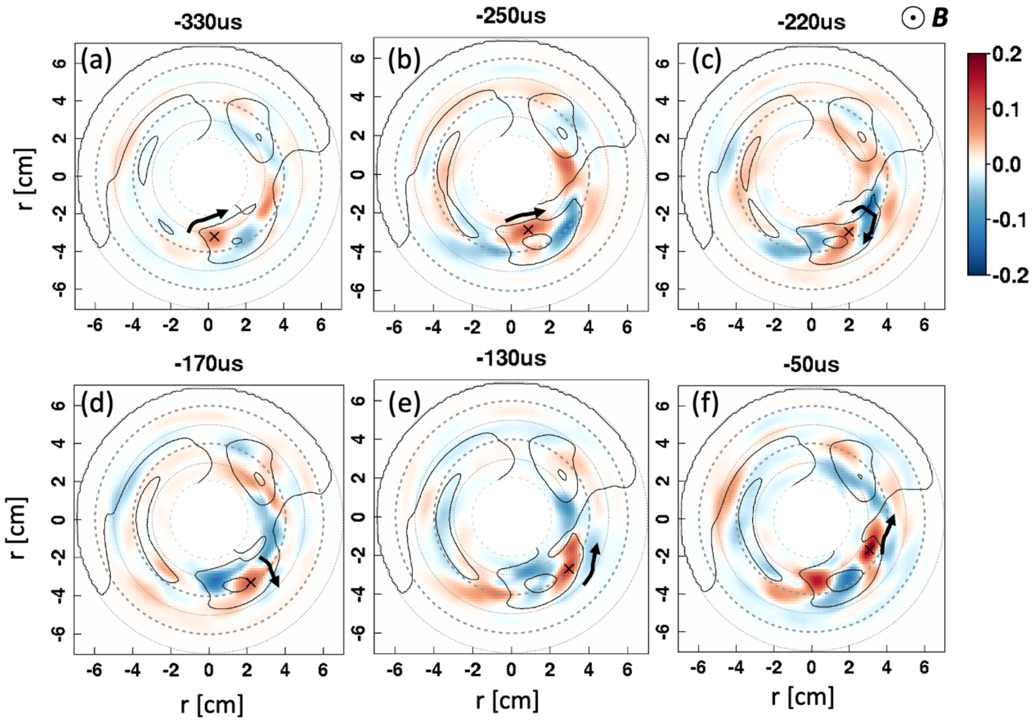

Figure 4. The instantaneous two-dimensional packet of finer-scale fluctuations at (a) $\tau = -330\,\mu$s, (b) $\tau = -250\,\mu$s, (c) $\tau = -220\,\mu$s, (d) $\tau = -170\,\mu$s, (e) $\tau = -130\,\mu$s, and (f) $\tau = -50\,\mu$s. The filled contour indicates the potential (ϕ) of the packet of finer-scale fluctuations and the contour lines indicates the potential of the waves and the solitary vortex. The cross-mark represents the instantaneous potential peak of the finer-scale fluctuations. The arrows indicate the guides of the propagating fluctuation peak.

the potential of the packet of finer-scale fluctuations. The contour lines indicate the potential of the waves and the solitary vortex. The cross mark in each figure indicates the location of the peak of the finer-scale fluctuations at each given moment. The arrow in the figure illustrates the propagation direction of the peak. The movement of the cross marks in time shows that the trajectory of the peaks is particularly radially varying, indicating that they are trapped in the solitary vortex.

The temporal evolution of the potential peak trajectories of the finer-scale fluctuation is explained in figure 5. The red-purple cross-lines in figure 5(a) indicate the radial and azimuthal profile axes of the solitary vortex shown in (b) and (d) on the Cartesian coordinate. The figure 5(b) or (d) shows the potential profiles of the solitary vortex in the radial or azimuthal direction when $\theta' = 0.84$ rad $(2\pi)^{-1}$ or $r = 3.5$ cm. The figures 5(c) or (e) indicates the peak trajectory in the radial or azimuthal direction of the potential of finer-scale fluctuations. Blue or red hatched areas each indicate the trajectory of the same peak, indicating two trappings. The peak meanders from 3 to 4 cm in the radial direction. In the azimuthal direction, it propagates in the electron diamagnetic direction, but pauses $\sim 5 \times 10^{-2}$ ms around $\theta' = 0.85$ rad $(2\pi)^{-1}$ when the peak moves radially. The trapping time of the packet of finer-scale fluctuations in the solitary vortex is 2×10^{-1}–3×10^{-1} ms.

7. Comparison with theoretical evaluation

The typical time scale of the finer-scale fluctuations circulating around the solitary vortex is close to the bounce time predicted by the trapping theory in a semi-quantitative manner [14, 15]. Using a theoretical evaluation of the bounce frequency for a wave packet trapped in a vortex to the conditions of this study yields $\omega_b = \sqrt{2k_\theta^2 q_r^2 \rho^4 V_G V_*^{-1} (1 + k_\theta^2 \rho^2)^{-2}} \cdot V_* \rho^{-1} \sim 2 \times 10^4$ rad s^{-1}, where k_θ is the azimuthal wavenumber of the finer-scale fluctuations, q_r is the radial wavenumber of the solitary vortex, V_G is the $E \times B$ velocity of the solitary vortex and V_* is the diamagnetic drift velocity; the parameters are $k_\theta \rho \sim 4 \times 10^{-1}$, $q_r \rho \sim 4 \times 10^{-1}$, $V_G V_*^{-1} \sim 1$ and $V_* \sim 1 \times 10^3$ m s^{-1}. The evaluated trapping time is $2\pi/\omega_b \sim 3 \times 10^{-1}$ ms, which is close to the experimental value (2×10^{-1}–3×10^{-1} ms). It is noted that the aforementioned theory is based on one-dimensional analysis; the inhomogeneity of the solitary vortex in the azimuthal direction is not taken into account.

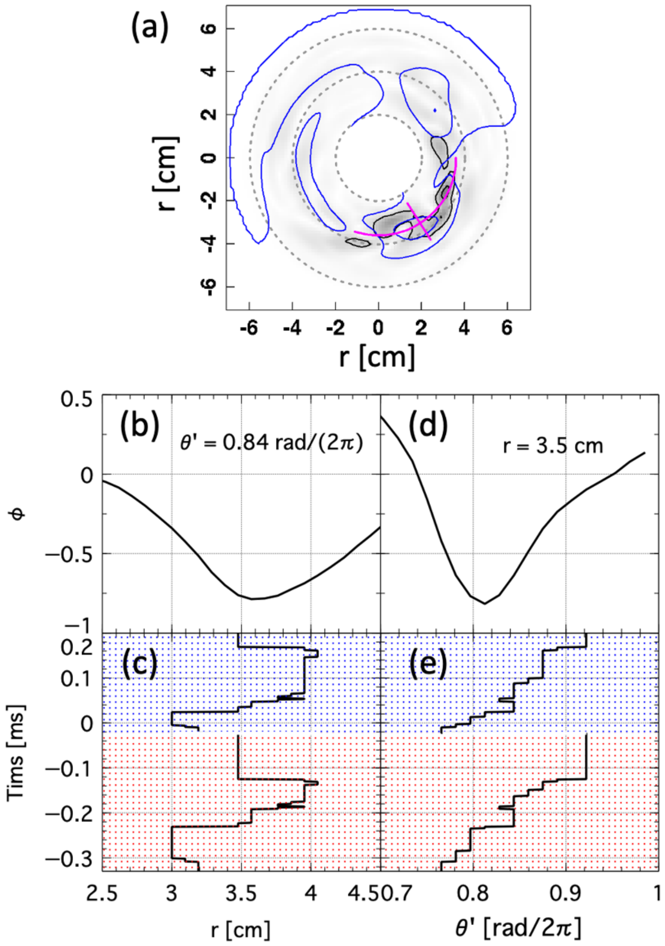

Figure 5. Peak propagation of finer-scale fluctuations in the cylindrical coordinate system. (a) The radial and azimuthal axes of the solitary vortex are shown in (b) and (d) on the Cartesian coordinates (red-purple cross-lines). The contour lines show the potential fluctuation of the waves and the solitary vortex. The filled contour represents the amplitude of the finer-scale fluctuations. (b) The radial profile of the solitary vortex at a azimuthal condition ($\theta' = 0.84\,\mathrm{rad}\,(2\pi)^{-1}$). (c) Peak propagation in the radial direction of the packet of finer-scale fluctuations. The ranges in which the same peaks propagate are indicated by the red or blue hatching region, respectively. (d) Azimuthal profile of the solitary vortex at $r = 3.5$ cm condition. (e) Peak propagation in the azimuthal direction of the finer-scale fluctuations.

8. Summary

In conclusion, turbulence excitation experiments were conducted in a linear magnetized plasma. Frequency filters and SVD were used to differentiate among zonal flows, drift wave-type modes, and solitary vortex and packet of finer-scale fluctuations. A modified template method was used to reconstruct time-varying two-dimensional cross-sectional structures. Peak tracking of the packet of finer-scale fluctuations revealed that fluctuations are observed to be trapped by the solitary vortex, particularly in the radial direction. The trapping times observed ranging from 0.2 to 0.3 ms, which is consistent with the one-dimensional theoretical evaluation.

Data availability statement

The data cannot be made publicly available upon publication because they are not available in a format that is sufficiently accessible or reusable by other researchers. The data that support the findings of this study are available upon reasonable request from the authors.

Acknowledgments

This work has been supported by the grant-in-aid for Scientific Research of JSPS KAKENHI (Grant Numbers JP17K14897, JP17H06089, JP15H02335, JP15H02155, JP21K03513 and JP21K03508), by the Collaborative Research Programme of Research Institute for Applied Mechanics, Kyushu University, by the Shimadzu Science Foundation, by the NIFS Collaboration Research program (NIFS17KOCH002), by the Agence Nationale de la Recherche for the project GRANUL (ANR-19-CE30-0005) and by the Asada Science Foundation.

Conflict of interest

The authors declare no competing financial interests.

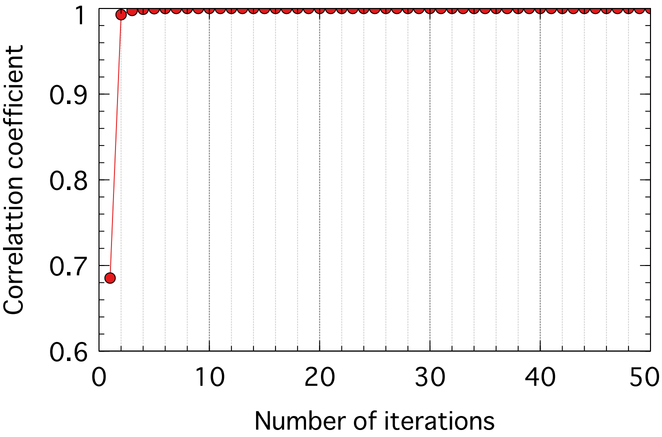

Figure A1. Correlation coefficient of the reference waveform versus number of iterations.

Appendix A. Convergence of two-dimensional reference waveform

The convergence of the reference waveform was validated using the correlation coefficient as it was iteratively refined. Figure A1 displays this correlation coefficient shown against the number of iterations. Specifically, the iteration number refers to the correlation between successive reference waveforms. For instance, the 2nd iteration point on the graph represents the correlation coefficient between the 1st (figure 2(b)) and 2nd (figure 2(c)) reference waveforms. The correlation coefficient reached 1 at the 8th iteration or more. This indicates that the reference waveform is in perfect agreement with the previous reference waveform at the 8th iteration or more.

Appendix B. Two-dimensional reconstruction with conditional averaging [20]

Figure B1 shows the method used for timing detection and for determining the conditions during conditional averaging. Figure B1(a) displays the spatio-temporal I_{is} with the Galilean transform applied to the azimuthal probe array data. This covers a partial azimuthal range of θ' =0.78–1.0 rad $2\pi^{-1}$, which includes the solitary vortex and the packet of finer-scale fluctuations. In figure B1(b), the cross-correlation function between I_{is} and the reference waveform (as seen in figure 2(e)) is depicted, with the correlation peaks highlighted by red points. The reference waveform is centered at $\tau = 0$, a point when the density of the solitary vortex and the packet of finer-scale fluctuations reaches its peak within the azimuthal probe array data, thus the correlation peak is observed at this timing. As shown in section 3, the waves, which include the drift wave-type mode and its harmonics, propagate in the electron diamagnetic direction. The timing of these correlation peaks and this propagation (shown in figure B1(c)) can be matched based on the azimuthal angle. On the other hand, the position of the radially movable probe is fixed at a specific azimuthal position. Therefore, the timing and relative azimuthal location (to the waves) of the radially movable probe can be determined similarly. Based on correlation peak timings, values (ϕ and $\tilde{I}_{\mathrm{is}}/\bar{I}_{\mathrm{is}}$) were obtained from the radially movable probe located at a particular radial position (as shown in figure B1(d), only ϕ is described as an example). For example, at the timing of the correlation peaks in the figure, $t_0(i)$, relative azimuthal location of radially movable probe, θ_i, was ascertained. In turn, $\phi(t_0(i), r)$ was also obtained by the radially movable probe. Consequently, ϕ is provided under conditions based on r and θ_i, relative to the waves.

The method of conditional averaging for two-dimensional reconstruction is illustrated in figure B2, taking the timings of $t_0(i)$ and $t_0(i+1)$ in figure B1 as examples. Figures B2(a) and (b) show the relative two-dimensional positions, θ_i and θ_{i+1}, of the radially movable probe at the times $t_0(i)$and $t_0(i+1)$, respectively, in relation to the azimuthal angles of the waves. Setting these timings as $\tau = 0$, transformations are applied such that $\tau = t - t_0(i)$ and $\tau = t - t_0(i+1)$. This approach facilitates the determination of ϕ in two-dimensional space at $\tau = 0$ for the radial position (r) and relative azimuthal angles θ_i or θ_{i+1} as depicted in figure B2(c). Given that the waves propagation angle around $\tau = 0$ while the movable probe remains stationary, the relationship between the propagating structures at time $\tau = \xi$ can be visualized, as in figure B2(d). Figure B2(e) demonstrates the azimuthal relationship of τ dependence between the propagating structure and the movable probe. This relationship stems from the propagation of the waves during the Galilean transformation applied to the azimuthal probe array data. The orange lines in figure B2(e) denote the peaks recognized before and after the timing $t_0(i)$ as shown in figure B2(a), while the purple lines represent the peaks observed before and after the timing $t_0(i+1)$ as illustrated in figure B2(b). The positions of these orange and purple lines align with the potential ϕ values derived from the movable probe, as shown in figures B2(f) and (g). Since these values are tied to specific radii (r), the temporal sequence of ϕ in a two-dimensional setting was reconstructed by pinpointing the azimuthal angles corresponding to the various radial positions (0.5 cm intervals) and correlation peaks. In total, 2596 correlation peaks were identified, which, when conditionally averaged, spanned the entire region, enabling the reconstruction of the two-dimensional structure.

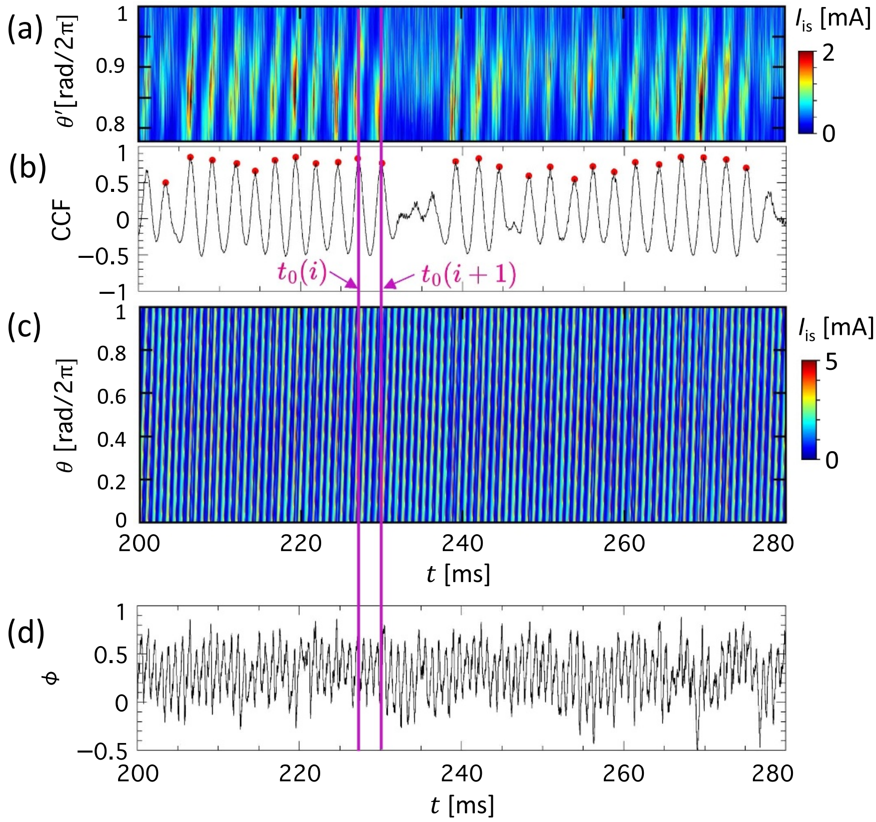

Figure B1. (a) A spatio-temporal I_{is} of a partial azimuthal range, $\theta' = 0.78–1.0\,\mathrm{rad}\,2\pi^{-1}$, from the azimuthal probe array. (b) Cross-correlation function (CCF) between (a) and the reference waveform (figure 2(e)), where the $t_0(i)$ and the $t_0(i+1)$ are the time at the ith correlation peaks. (c) Corresponding spatio-temporal I_{is} from the azimuthal probe array before the Galilean transformation. (d) A potential of movable probe installed at a radial and a azimuthal position measured simultaneously.

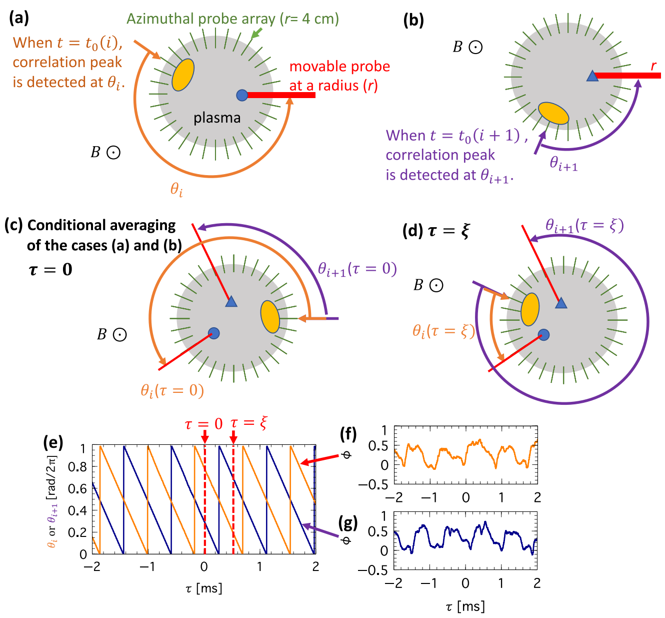

Figure B2. (a) and (b) The relative azimuthal positions of the movable probe in two-dimensional space at time points $t_0(i)$ and $t_0(i+1)$, respectively. (c) The two-dimensional position of the movable probe at $\tau = 0$, relative to the propagating waves depicted in (a) and (b). (d) Two-dimensional relationships at timing $\tau = \xi$. (e) The τ-dependence of azimuthal positional relationships. The orange and purple lines represent the positions θ_i and θ_{i+1}, respectively. (f) and (g) The respective τ-dependencies of ϕ as measured by the movable probe.

ORCID iDs

Hiroyuki Arakawa https://orcid.org/0000-0001-9793-099X
Makoto Sasaki https://orcid.org/0000-0001-6835-1569
Shigeru Inagaki https://orcid.org/0000-0002-4808-857X
Maxime Lesur https://orcid.org/0000-0001-9747-5616
Yusuke Kosuga https://orcid.org/0000-0002-4075-5542
Tatsuya Kobayashi https://orcid.org/0000-0001-5669-1937
Fumiyoshi Kin https://orcid.org/0000-0001-6248-8695
Kimitaka Itoh https://orcid.org/0000-0003-3873-4766

References

[1] Diamond P H, Itoh S-I, Itoh K and Hahm T S 2005 *Plasma Phys. Control. Fusion* **47** 35–161
[2] Itoh K, Hallatschek K, Itoh S-I, Diamond P H and Toda S 2005 *Phys. Plasmas* **12** 062303
[3] Fujisawa A 2009 *Nucl. Fusion* **49** 013001
[4] Nakata M, Watanabe T-H and Sugama H 2012 *Phys. Plasmas* **19** 022303
[5] Yan Z, McKee G R, Fonck R, Gohil P, Groebner R J and Osborne T H 2014 *Phys. Rev. Lett.* **112** 125002
[6] Conway G D, Smolyakov A I and Ido T 2021 *Nucl. Fusion* **62** 013001
[7] Tynan G R, Fujisawa A and McKee G 2009 *Plasma Phys. Control. Fusion* **51** 113001
[8] Manz P, Xu M, Thakur S C and Tynan G R 2011 *Plasma Phys. Control. Fusion* **53** 095001
[9] Hong R, Li J C, Thakur S C, Hajjar R, Diamond P H and Tynan G R 2018 *Phys. Rev. Lett.* **120** 205001
[10] Carter T A and Maggs J E 2009 *Phys. Plasmas* **16** 012304
[11] Brandt C, Thakur S C, Light A D, Negrete J J R and Tynan G R 2014 *Phys. Rev. Lett.* **113** 265001
[12] Schaffner D A, Carter T A, Rossi G D, Guice D S, Maggs J E, Vincena S and Friedman B 2012 *Phys. Rev. Lett.* **109** 135002
[13] Ma J T, Xiao W W, Wang C Y, Zhong W J and Wali N 2023 *Phys. Plasmas* **30** 072301
[14] Kaw P, Singh R and Diamond P H 2001 *Plasma Phys. Control. Fusion* **44** 51
[15] Sasaki M, Itoh K, Hallatschek K, Kasuya N, Lesur M, Kosuga Y and Itoh S-I 2017 *Sci. Rep.* **7** 1–7
[16] Sasaki M, Kobayashi T, Itoh K, Kasuya N, Kosuga Y, Fujisawa A and Itoh S-I 2018 *Phys. Plasmas* **25** 012316
[17] Garbet X, Panico O, Varennes R, Gillot C, Dif-Pradalier G, Sarazin Y, Grandgirard V, Ghendrih P and Vermare L 2021 *Phys. Plasmas* **28** 042302
[18] Sasaki M, Itoh K, McMillan B F, Kobayashi T, Arakawa H and Chowdhury J 2021 *Phys. Plasmas* **28** 112304
[19] Sasaki M, Arakawa H, Kobayashi T, Kin F, Kawachi Y, Yamada T and Itoh K 2021 *Phys. Plasmas* **28** 102304
[20] Arakawa H *et al* 2019 *Phys. Plasmas* **26** 052305
[21] Arakawa H *et al* 2022 *Plasma Fusion Res.* **17** 1301106
[22] Nagashima Y *et al* 2009 *Phys. Plasmas* **16** 020706
[23] Inagaki S *et al* 2014 *Plasma Fusion Res.* **9** 1201016
[24] Henry E R and Hofrichter J 1992 [8] Singular value decomposition: application to analysis of experimental data *Numerical Computer Methods* (*Methods in Enzymology*) vol 210 (Academic) pp 129–92
[25] Sasaki M, Kobayashi T, Dendy R O, Kawachi Y, Arakawa H and Inagaki S 2021 *Plasma Phys. Control. Fusion* **63** 025004